PNAS RESEARCH ARTICLE | APPLIED PHYSICAL SCIENCES

Detecting DNA translocation through a nanopore using a van der Waals heterojunction diode

Sihan Chen[a], Siyuan Huang[b], Jangyup Son[b,1,2,3], Edmund Han[c], Kenji Watanabe[d], Takashi Taniguchi[e], Pinshane Y. Huang[c,f], William P. King[a,b,c,f,g], Arend M. van der Zande[a,b,c,f,4], and Rashid Bashir[a,b,c,f,g,h,i,j,4]

Affiliations are included on p. 7.

Edited by Mehmet Toner, Massachusetts General Hospital, Charlestown, MA; received October 25, 2024; accepted April 4, 2025 by Editorial Board Member John A. Rogers

A long-unrealized goal in solid-state nanopore sensing is to achieve out-of-plane electrical sensing and control of DNA during translocation, which is a prerequisite for base-by-base ratcheting that enables DNA sequencing in biological nanopores. Two-dimensional (2D) heterostructures, with their capability to construct out-of-plane electronics with atomic layer precision, are ideal yet unexplored candidates for use as electrical sensing membranes. Here, we demonstrate a nanopore architecture using a vertical 2D heterojunction diode consisting of p-type WSe_2 on n-type MoS_2. This diode exhibits rectified interlayer tunneling currents modulated by ionic potential, while the heterojunction potential reciprocally rectifies ionic transport through the nanopore. We achieve concurrent detection of DNA translocation using both ionic and diode currents and demonstrate a 2.3-fold electrostatic slowing of average translocation speed. Encapsulation layers enhance chemical and mechanical stability and durability while preserving the spatial resolution of atomically sharp 2D heterointerface for sensing. These results establish a paradigm for out-of-plane electrical sensing of single biomolecules.

nanopore | van der Waals heterojunction | DNA | single molecule | ion transport

Nanopore sensors, with a sensing volume comparable to the analyte size, are a powerful tool for single-biomolecule analysis (1, 2). Eighteen years ago, IBM introduced the idea of out-of-plane electrical sensing and control using a "DNA transistor" (3). This design employs electrodes separated by a thin dielectric to control and sense DNA translocation through a nanopore. However, limitations in thin-film processes hindered the scaling of the transistor to the molecular thicknesses needed for sensing (4). Vertically stacked two-dimensional (2D) heterostructures provide layer-by-layer control to construct out-of-plane electronics (5, 6), opening possibilities beyond single 2D materials for sensing with out-of-plane electric fields and interlayer currents. Unlike three-dimensional (3D) diodes with a depletion region, vertical 2D junctions exhibit an atomically sharp energy band discontinuity at their heterointerface (6), which represents the ultimate limit for DNA transistors, with the conducting layers separated by only an angstrom-sized van der Waals gap. These attributes make vertical 2D heterojunction diodes an ideal candidate for use as electrical sensing membranes.

In this work, we present a nanopore architecture integrated with a vertical 2D heterojunction diode from p-type WSe_2 on n-type MoS_2, referred to as the HJD-NP sensor. We first electrically characterized the heterojunction to demonstrate the p-n diode behavior, then characterized the transport characteristics of both the ionic and diode channels in the absence of analytes, and finally demonstrated DNA sensing using an HJD-NP sensor. Three key advances from these proof-of-principle experiments include: i) concurrent detection of DNA translocation through a vertical diode nanopore using both ionic and diode currents, ii) slowing of DNA translocation via electrostatic interactions between the DNA and diode, and iii) rectified ionic transport controlled by heterojunction potential. These results highlight the potential of HJD-NP sensors for sensitive single-biomolecule analysis with high spatial resolution and extended interrogation time.

Results and Discussion

Nanopore Integrated with a Vertical 2D Diode. Fig. 1 presents the basic concept of the HJD-NP sensors for DNA sensing. As illustrated in Fig. 1*A*, a nanopore is formed in an electrically contacted 2D heterojunction, which consists of a p-type WSe_2 flake stacked on an n-type MoS_2 flake. This heterojunction forms an out-of-plane p-n diode. When a double-stranded DNA (dsDNA) molecule translocates through the nanopore under an

Significance

Nanopores are nanometer-sized openings that enable detailed analysis of molecular structures by analyzing individual biomolecules as they pass through. Solid-state nanopores integrated with local electronic sensors hold promise for high-throughput, label-free, single-molecule sensing. However, integrating solid-state nanopores with local electrical sensing modalities remains challenging, with successful implementations limited to in-plane architectures such as tunneling junctions and transistors. This work demonstrates the integration of a nanopore with a vertical two-dimensional heterojunction diode, enabling electrical sensing of DNA translocation through the nanopore via interlayer tunneling current, opening the possibility for out-of-plane electrical sensing and control of single biomolecules.

The authors declare no competing interest.

This article is a PNAS Direct Submission. M.T. is a guest editor invited by the Editorial Board.

[1]Present address: Functional Composite Materials Research Center, Korea Institute of Science and Technology, Wanju-gun 55324, Jeonbuk, Republic of Korea.

[2]Present address: Division of Nanoscience and Technology, Korea Institute of Science and Technology School, University of Science and Technology, Seoul 02792, Republic of Korea.

[3]Present address: Department of Jeonbuk National University-Korea Institute of Science and Technology Industry-Academia Convergence Research, Jeonbuk National University, Jeonju 54896, Jeonbuk, Republic of Korea.

[4]To whom correspondence may be addressed. Email: arendv@illinois.edu, or rbashir@illinois.edu.

This article contains supporting information online at https://www.pnas.org/lookup/suppl/doi:10.1073/pnas.2422135122/-/DCSupplemental.

Published May 1, 2025.

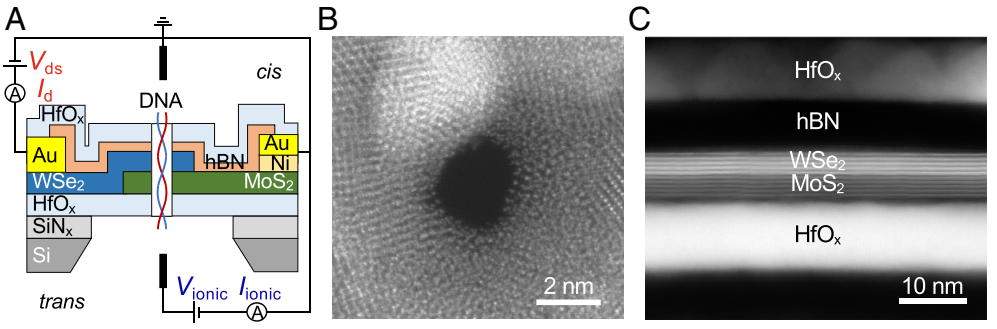

Fig. 1. Device architecture and structural characterization. (*A*) Schematic of device architecture and measurement setup of an HJD-NP, with n-type MoS_2 and p-type WSe_2. When a dsDNA molecule translocates through the nanopore, it induces changes in the interlayer current. (*B*) High-angle annular dark-field (HAADF) scanning transmission electron microscopy (STEM) image of an example nanopore drilled through a membrane stack. (*C*) Cross-sectional HAADF-STEM image of a representative device showing the membrane stack.

external ionic bias V_{ionic}, the sensor simultaneously interrogates the conventional ionic current I_{ionic} through the pore and the electrical current I_d across the diode under a drain-source bias V_{ds}.

The detailed device fabrication procedures are described in *Materials and Methods* and *SI Appendix*, Fig. S1. Briefly, we started the fabrication with HfO_x membranes formed by atomic layer deposition (ALD) (*SI Appendix*, Fig. S2), which is hydrophilic (7) and durable in salt solutions (8). Then we transferred 2 to 5 nm (2 to 7 layers) thick MoS_2 and WSe_2 flakes onto the membrane to form the heterojunction stack, with a 1 to 10 μm^2 overlap region. While thinner diodes are preferred for better spatial resolution, it remains challenging to fabricate working diodes from monolayer 2D semiconductors, primarily limited by p-type contacts (6). Therefore, we used few-layer structures instead of monolayers. Next, we fabricated n-type and p-type ohmic contacts to MoS_2 and WSe_2 using evaporated Ni/Au contacts and transferred Au contacts, respectively (*SI Appendix*, Fig. S3). Subsequently, we transferred a multilayer hBN flake to fully encapsulate the WSe_2/MoS_2 heterostructure (9). This hBN buffer layer preserves the electrical conductivity of p-type WSe_2 during ALD (10). Afterward, we deposited a layer of ALD HfO_x for electrical insulation and stable operation. Finally, we drilled a nanopore in the overlap region through the membrane stack using a focused electron beam in STEM mode, which minimizes electron-beam induced damage to electronic materials compared to TEM mode (11). Fig. 1*B* shows the STEM image of an example nanopore. Further details on nanopore drilling are provided in *SI Appendix*, *Supplementary Text 1* and Fig. S4.

We confirmed the structure of the heterojunction and cleanliness of the interface between layers with cross-section STEM. Fig. 1*C* shows a representative membrane stack, which consists of HfO_x, hBN, five-layer WSe_2, five-layer MoS_2, and HfO_x from top to bottom. The heterointerface between WSe_2 and MoS_2 is atomically clean, which is critical for efficient interlayer charge carrier transport (12). Raman microscopy in *SI Appendix*, Fig. S5 further suggests interlayer coupling between WSe_2 and MoS_2.

To use the heterojunction current for sensing, we must first understand the electrical transport properties and sensitivity of the van der Waals heterojunction. Due to defects incorporated during synthesis and environmental interactions (13, 14), few-layer WSe_2 is lightly p-doped while few-layer MoS_2 is heavily n-doped, as confirmed by FET transport measurements in *SI Appendix*, Fig. S3. Vertical stacking of *p*-WSe_2 on n^+-MoS_2 forms a p–n diode with a type-II energy band alignment (Fig. 2*A*). Under forward bias, I_d is dominated by interlayer recombination between the majority carriers of WSe_2 and MoS_2 over diffusion current, and I_d is maximized when the hole density of WSe_2 and the electron density of MoS_2 are balanced (5, 15). Fig. 2*B* shows the I_d–V_{ds} curve of an example HJD-NP sensor measured in dry air in dark, exhibiting forward rectification characteristic of a p-n diode.

However, unlike an ideal vertical p-n diode, the total van der Waals heterojunction resistance R_{ds} also includes series resistances (Fig. 2*C*), which consist of the contact resistances to WSe_2 and MoS_2, as well as the channel resistances of WSe_2 and MoS_2 in both the non-overlapping and overlapping regions. We establish that the p-n junction is the dominant resistance in the system using photocurrent microscopy (*SI Appendix*, Fig. S6*A*). Since photocurrent is sensitive to the electric field gradient within the junction, its magnitude is greatest at the junction with the highest resistance. Fig. 2*D* shows the photocurrent map for an example device at $V_{ds} = 0$ mV. The strongest photo response came from the MoS_2/WSe_2 overlap region, confirming the formation of a p-n junction (5). *SI Appendix*, Fig. S6*B* shows additional photocurrent maps at $V_{ds} \neq 0$ mV for this device, which also supports this finding. Other heterojunction devices exhibited a strong photo response from the Au–WSe_2 junction or the WSe_2 channel region (*SI Appendix*, Fig. S6 *C* and *D*) and/or non-rectifying I_d–V_{ds} characteristics (*SI Appendix*, Fig. S7). We screened all diodes using photocurrent microscopy and selected those with both strong rectification and a dominant photocurrent in the overlap region for sensing measurements.

Next, we studied the device behavior in an ionic environment to identify the optimal measurement parameters for electrical sensing. There are two control knobs for device operation, namely V_{ionic} and V_{ds}. Fig. 2*E* illustrates the coupling between the ionic and diode channels, which is comparable to that of FET-nanopore sensors (16–20), except here the sensing element is a vertical van der Waals heterojunction diode rather than a planar FET. The ionic voltage controls the heterojunction current transport via electrostatic gating. As shown in Fig. 1*A*, the backside HfO_x serves as the gate dielectric, while the front side is grounded to minimize electrochemistry. Fig. 2 *F* and *G* shows the output and transfer characteristics of the heterojunction in an HJD-NP device, respectively. The current rectification improved with a more negative V_{ionic}, indicating that the *p*-WSe_2 partly limits the charge transport in the heterojunction and that the contact and channel resistances of the n^+-MoS_2 are comparably small. Liquid gating is insensitive to salt concentrations, as the gate capacitance of the electric double layers far exceeds that of the backside HfO_x. The FET transport characteristics of a backgated *p*-WSe_2/n^+-MoS_2 heterojunction on a SiO_2/Si substrate also supports these findings (*SI Appendix*, Fig. S8). Therefore, *p*-WSe_2/n^+-MoS_2 heterojunction under forward bias can be modeled as a vertical p-n diode in series with an additional p-FET. We assume a uniform electric potential of αV_d for WSe_2 and 0 mV for MoS_2 in the overlap region, where α is

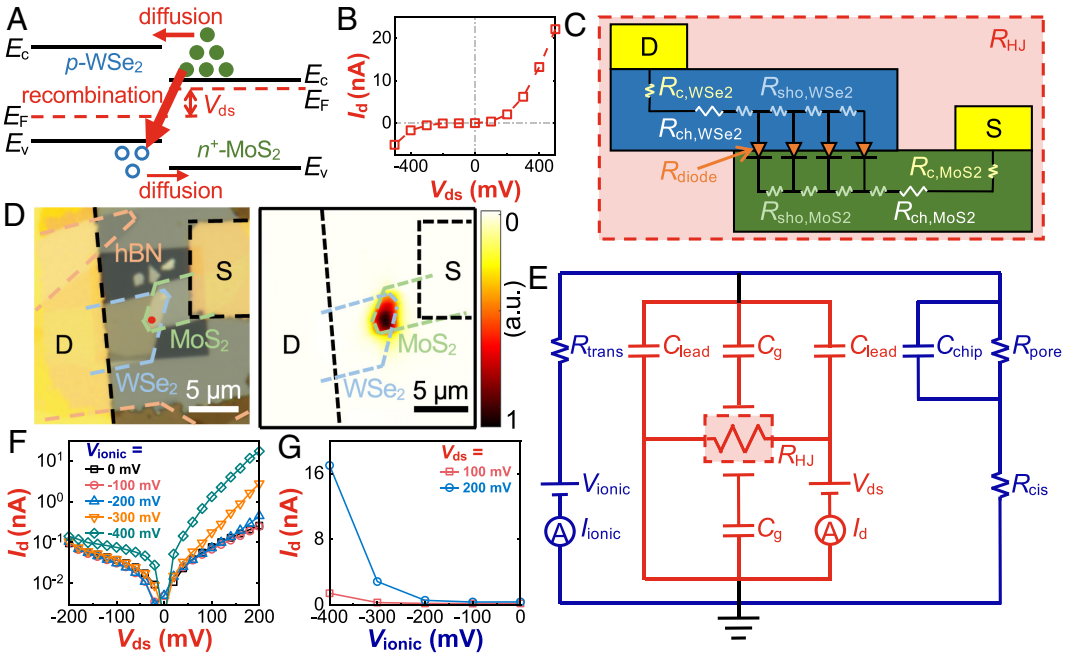

Fig. 2. Equivalent circuit diagrams and electrical characterization. (*A*) The ideal band diagram of a vertical *p*-WSe_2/n^+-MoS_2 diode under forward V_{ds} bias. The current due to interlayer recombination between the majority carriers of WSe_2 and MoS_2 dominates over the diffusion current (5, 15). (*B*) I_d–V_{ds} curve of an example HJD-NP sensor measured in dry air in dark. (*C*) Equivalent circuit of the van der Waals heterojunction. R_{HJ} is the total resistance of the heterojunction. $R_{c,WSe2}$ and $R_{c,MoS2}$ are the contact resistances to WSe_2 and MoS_2, respectively. $R_{ch,WSe2}$ and $R_{ch,MoS2}$ are the channel resistances of WSe_2 and MoS_2 in the non-overlapping region, respectively. $R_{sho,WSe2}$ and $R_{sho,MoS2}$ are the sheet resistances of WSe_2 and MoS_2 in the overlapping region, respectively. R_{diode} is the interface resistance between WSe_2 and MoS_2 per unit area. (*D*) Optical image (*Left*) and corresponding photocurrent map (*Right*) at V_{ds} = 0 mV of an example HJD-NP. The red dot indicates the location of the nanopore. (*E*) Equivalent circuit of an HJD-NP. R_{cis} and R_{trans} are the resistances of the salt solution in the *cis* and *trans* chambers, respectively, C_{chip} is the chip capacitance, R_{pore} is the nanopore resistance, C_{lead} is the capacitance between the electrolyte and the contact leads on the drain or source side, and C_g is the capacitance between the electrolyte and the heterojunction. The ionic channel is shown in blue and the diode channel in red. (*F*) Output and (*G*) Transfer curves of the heterojunction in an HJD-NP under liquid gating in a 1 M LiCl buffer.

the ratio of the vertical p-n diode resistance to the total heterojunction resistance. Consequently, applying a more negative V_{ionic} could further reduce the series resistances of the heterojunction in an HJD-NP, thereby enhancing the sensitivity of electrical sensing.

Electrical Rectification of Ionic Current. Fig. 3 examines the opposite situation of how the diode potential affects ionic transport. Fig. 3 *A* and *B* show the output and transfer curves of ionic transport of a liquid-gated HJD-NP with a pore size d_{pore} of 4.0 ± 0.3 nm in 10 mM KCl. The ionic I–V characteristics were modulated by V_{ds}. Specifically, i) $|I_{ionic}|$ increased (decreased) when V_{ds} and V_{ionic} had opposite (the same) polarities. ii) I_{ionic} exhibited greater variation with V_{ds} under forward bias compared to reverse bias. iii) $|I_{ionic}|$ was most rectified at the most negative V_{ionic}.

To understand the mechanism behind the ionic current control by V_{ds}, we measured four HJD-NP sensors with d_{pore} from 1.1 ± 0.3 nm to 7.7 ± 0.3 nm and KCl concentrations c_{KCl} from 1 mM to 1 M (*SI Appendix*, Fig. S9). Fig. 3*C* plots the ionic current on/off ratio $I_{ionic,ON}/I_{ionic,OFF}$ and the maximum change in ionic current $I_{ionic,ON} - I_{ionic,OFF}$ versus d_{pore} in a 10 mM KCl buffer, where $I_{ionic,ON}$ and $I_{ionic,OFF}$ were measured at V_{ds} = ±200 mV. Fig. 3*D* plots $I_{ionic,ON}/I_{ionic,OFF}$ versus c_{KCl} for two nanopore devices, where $I_{ionic,ON}$ and $I_{ionic,OFF}$ were measured at V_{ds} = ±100 mV. The data show that $I_{ionic,ON}/I_{ionic,OFF}$ decreased significantly with d_{pore} to the power of –1.25 ± 0.10 and slightly with c_{KCl} to the power of –0.03 to –0.06. In addition, $I_{ionic,ON} - I_{ionic,OFF}$ increased sublinearly with d_{pore}. Fig. 3*E* shows the cyclic changes in I_{ionic} as V_{ds} switched between ±200 mV at a fixed V_{ionic} of –400 mV, demonstrating stability and repeatability.

There are two common mechanisms for modulating the ionic currents with interlayer potentials: i) edge electrochemistry at the nanopore, and ii) electrostatic interactions. Both applied biases, $|V_d - V_{ionic}|$ and $|V_s - V_{ionic}|$, were capped at 600 mV, below the 800-mV onset for electrochemical reactions in monolayer MoS_2 and WSe_2 in 1 M KCl (21, 22). If edge chemistry dominated, then $I_{ionic,ON} - I_{ionic,OFF}$ would increase linearly with the surface area of the pore edges A_{pore}, as the electrochemical current increases linearly with A_{pore} (23). However, this predicted linear relationship between $I_{ionic,ON} - I_{ionic,OFF}$ and A_{pore} contradicts the observed trend (*SI Appendix*, Fig. S10*A*), suggesting that edge chemistry did not play a dominant role. Additionally, $I_{ionic,ON} - I_{ionic,OFF}$ for one HJD-NP sensor with a pore size of 2.2 ± 0.3 nm remained relatively constant as c_{KCl} increased from 1 mM to 100 mM (*SI Appendix*, Fig. S10*B*), confirming negligible electrochemistry.

After ruling out edge electrochemistry, we attribute the control of ionic transport by V_{ds} to electrostatic interactions between the biased heterojunction and the ions within the nanopore channel. There are two possible origins of electrostatic modulation of the ionic transport: i) interlayer voltage drop across the vertical heterojunction (24, 25), and ii) field-effect gating like an embedded electrode (26, 27). We ruled out the effect of the vertical potential drop, as reversing the heterojunction stacking sequence, and hence the direction of the electric field from V_{ds}, did not reverse the induced ionic transport (*SI Appendix*, Fig. S9 *C* and *D*). Therefore, we attribute the control of ionic transport by V_{ds} to field-effect gating, which effectively explains the observed modulation of ionic transport by V_{ds} (*SI Appendix*, *Supplementary Text 2*) and can be leveraged for dynamic control of DNA translocation speed (28–31).

We acknowledge that other mechanisms could also account for the modulation of the ionic currents by interlayer potentials, such as chemical modifications of the pore edges, changes in the hydration structure of water, or changes in ion mobility in the vicinity of the diode junction. Such phenomena could reduce the effective

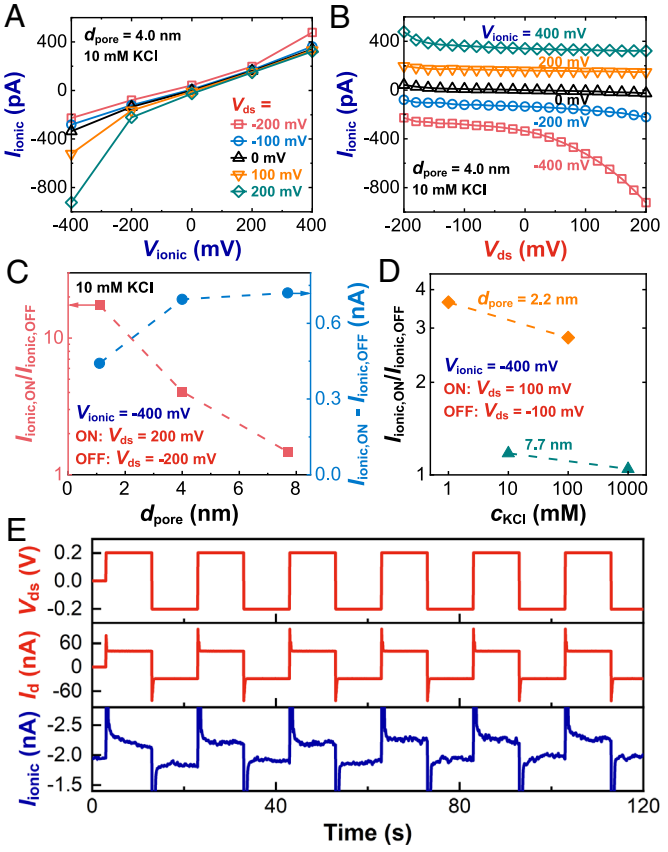

Fig. 3. Ionic current modulation. (*A*) Output and (*B*) Transfer curves of the ionic transport of an HJD-NP with a d_{pore} of 4.0 ± 0.3 nm under varying V_{ds}. The heterojunction stack consists of 3.4 nm thick WSe_2 on top of 3.8 nm thick MoS_2. (*C*) Ionic current on/off ratio $I_{ionic,ON}/I_{ionic,OFF}$ and the maximum difference in ionic current $I_{ionic,ON} - I_{ionic,OFF}$ versus d_{pore} at V_{ionic} = −400 mV in a 10 mM KCl buffer. ON state: V_{ds} = 200 mV; OFF state: V_{ds} = −200 mV. (*D*) $I_{ionic,ON}/I_{ionic,OFF}$ versus c_{KCl} at V_{ionic} = −400 mV for two nanopore devices. ON state: V_{ds} = 100 mV; OFF state: V_{ds} = −100 mV. (*E*) Response of I_d and I_{ionic} of an HJD-NP to cyclic switching of V_{ds} between ±200 mV at a fixed V_{ionic} of −400 mV. The pore size was 7.7 ± 0.3 nm, and the buffer was 10 mM KCl.

diameter of the pore, with a more pronounced impact on small pores compared to larger ones. Further simulations are required to evaluate and identify specific mechanisms.

Additionally, we modeled ion transport in HJD-NP with a floating diode (*SI Appendix*, *Supplementary Text 3*, Table S1, and Fig. S11). This ionic model was used to estimate d_{pore} in liquid measurements based on the measured ionic conductance. We also examined the effect of grounding the diode on ionic transport (*SI Appendix*, Fig. S12). The ionic I–V curves before and after grounding the diode remained linear and nearly identical, indicating negligible leakage and that connecting the diode with V_{ds} = 0 mV does not affect ion transport.

Electrical Sensing of DNA. In Fig. 4, we demonstrate the electrical sensing of dsDNA using an HJD-NP, with the measurement setup depicted in Fig. 1*A*. Both the *cis* and *trans* chambers were filled with 10 mM KCl. 50 nM of 2,686 bp circular dsDNA was added into the *trans* chamber. V_{ionic} was varied from −300 to −400 mV, while V_{ds} was varied from 0 to 200 mV. As expected, DNA translocation was detected only in the ionic channel at V_{ds} = 0 mV (*SI Appendix*, Fig. S13 *A* and *B*). In contrast, DNA translocation was simultaneously detected in both ionic and diode channels at V_{ds} = 200 mV (*SI Appendix*, Fig. S13 *C* and *D*). Fig. 4*A* shows example traces of these concurrently detected events. Both the ionic and diode currents increased upon DNA translocation. The increase of the ionic current is a signature of DNA translocation in dilute salt solutions like 10 mM KCl, where the transport of the counterions of DNA dominates over bulk ion transport (32, 33). The simultaneous increase of the diode current suggests the presence of DNA inside the nanopore channel reduced the diode resistance.

When a dsDNA molecule translocates through an HJD-NP, two non-capacitive electrical sensing mechanisms contribute to changes in I_d (Fig. 4*B*): i) charge sensing and ii) volumetric blockade-based sensing. The negative charges from the translocating DNA strand reduce the charge imbalance at the heterointerface of p-WSe_2/n^+-MoS_2, leading to an increase in I_d (*SI Appendix*, *Supplementary Text 4*). Volumetric blockade–induced local potential change would otherwise lead to a decrease in I_d and therefore can be ruled out. The transconductance of this heterojunction was only 0.8 pA/mV (*SI Appendix*, Fig. S14). Based on analytical calculations and simulations (16, 18), we estimate a maximum potential change of 1 mV at the nanopore entrance, corresponding to a change in I_d of <1 pA. No capacitive signals were observed in the ionic or diode channel. Since R_{lead} exceeded 10 GΩ (*SI Appendix*, Fig. S15) and C_{lead} was only 9.2 pF (*Materials and Methods*), both capacitive crosstalk and direct leaking between the ionic and diode channels should be negligible (17, 18). Above all, we ascribe the observed increase in diode current upon DNA translocation to charge sensing.

A total of 409 concurrent events were detected at V_{ionic} = −300 mV, V_{ds} = 200 mV over 9.6 min, and 238 events at V_{ionic} = −400 mV, V_{ds} = 200 mV over 7.8 min, as shown in the scatterplots in Fig. 4 *C* and *D*. The current changes of the concurrent events detected in the ionic channel ΔI_{ionic} and the diode channel ΔI_{diode} are weakly correlated, with a Pearson's correlation coefficient of r^2 = 0.41 (Fig. 4*E*), suggesting different physical origins. Fig. 4*F* shows the scatterplots of the events detected in the ionic channel at V_{ionic} = −300, −400 mV, V_{ds} = 0 mV. The median and SD of the dwell times and current changes were extracted from these scatterplots and presented in Fig. 4 *G* and *H*. The details of data processing and analysis are in *Materials and Methods*. Notably, the median dwell time at V_{ionic} = −300 mV increased from 1.2 to 2.8 ms as V_{ds} increased from 0 to 200 mV. As V_{ionic} changed from −300 to −400 mV, ΔI_{ionic} increased by 12%, from 97 ± 18 to 109 ± 18 pA, while ΔI_{diode} increased by only 4%, from 129 ± 24 to 134 ± 24 pA. The ionic signal-to-noise ratio (SNR) was 3.5 to 3.6, while the diode SNR was 3.9 to 4.2. This diode SNR is comparable to the FET SNR of 2D FET-nanopore sensors (*SI Appendix*, Table S2). Both the ionic and diode channels exhibited similar noise levels (*SI Appendix*, Fig. S16).

Interestingly, the median dwell time increased with increasing V_{ds} regardless of V_{ionic}, suggesting that applying V_{ds} slowed the DNA translocation. Additionally, dwell time increased slightly with $|V_{ionic}|$, differing from conventional nanopore sensors at high salt concentrations with ionic bias alone, where dwell time decreases with $|V_{ionic}|$ (34). We ascribe the reduced DNA translocation speed to field-effect gating of the nanopore channel induced by the biased heterojunction. Specifically, as V_{ionic} becomes more negative and V_{ds} more positive, the effective gate potentials at the nanopore channel relative to WSe_2 and MoS_2, i.e., $|V_{ionic} - \alpha V_d|$ and $|V_{ionic}|$, both increase (29, 30). This gating effect on DNA translocation may remain significant even when the pore diameter substantially exceeds the Debye length (29, 30).

We also note the transport behavior of charged macromolecules at low salt concentrations may differ from that at high salt concentrations (35, 36), which could also contribute to the unconventional dependence of dwell time on $|V_{ionic}|$. In addition, acquiring additional DNA translocation events with increased

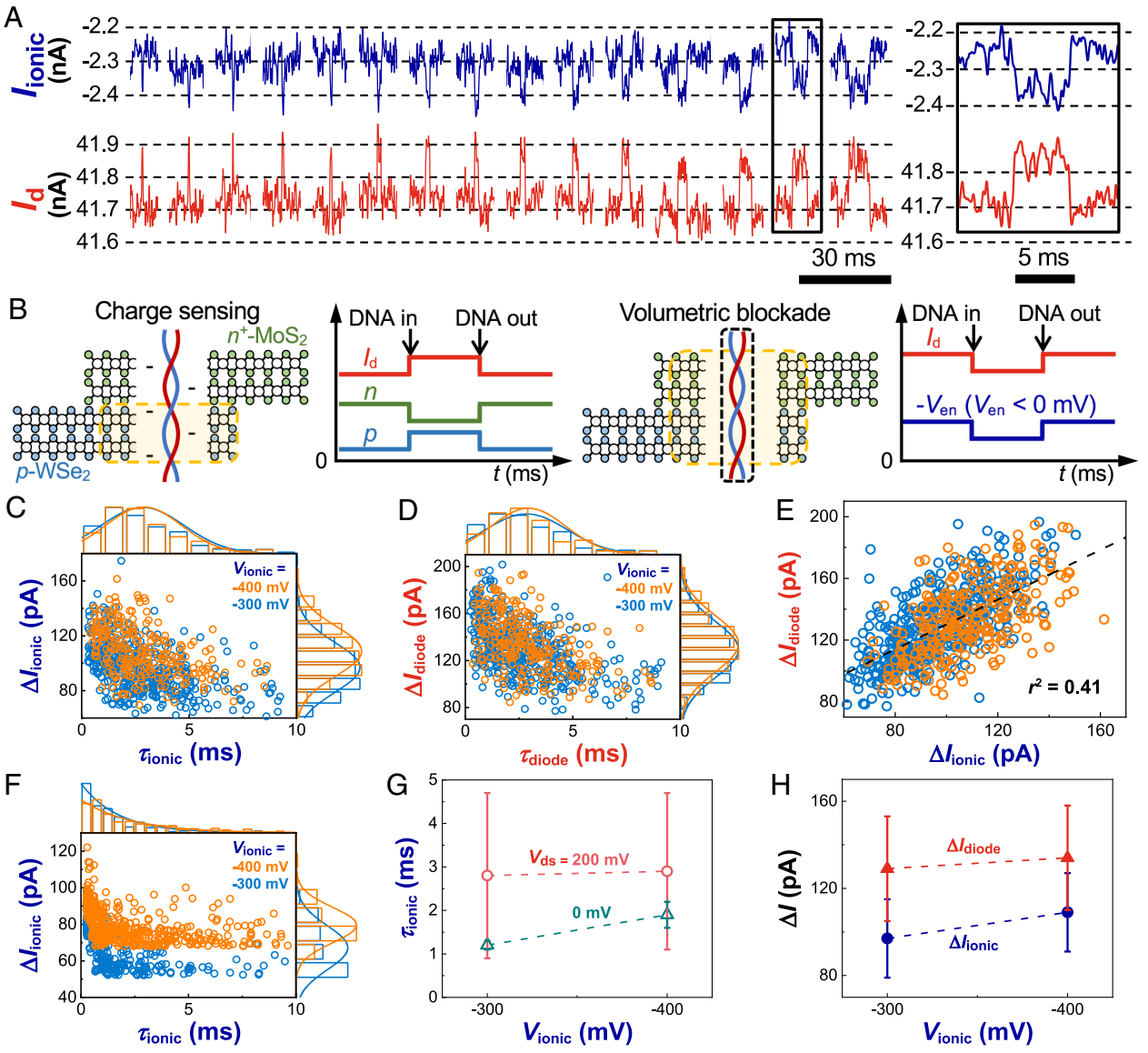

Fig. 4. Concurrent diode and ionic current sensing of DNA translocation. (*A*) Concatenated signal traces (*Left*) and zoom-in view of a single concurrent event (*Right*). V_{ionic} = −300 mV, V_{ds} = 200 mV. (*B*) Two potential electrical sensing mechanisms for detecting translocating dsDNA through a p-WSe_2/n^+-MoS_2 heterojunction nanopore: charge sensing and volumetric blockade-based sensing. In charge sensing, as negatively charged dsDNA enters the nanopore, it improves the balance between hole density p and electron density n at the heterointerface, leading to an increase in I_d. In volumetric blockade-based sensing, when a negative V_{ionic} is applied, the amplitude of the voltage at the nanopore entrance V_{en} decreases upon DNA translocation, resulting in a decrease in I_d. The sensitive region is shown in the golden zone. Scatterplots of the concurrent events detected in the (*C*) ionic channel and (*D*) diode channel, showing changes in ionic current ΔI_{ionic} and diode current ΔI_{diode}, as well as dwell times for both ionic τ_{ionic} and diode τ_{diode} signals. V_{ionic} = −300, −400 mV, V_{ds} = 200 mV. (*E*) Signal amplitude correlation between concurrent events in the ionic and diode channels. V_{ionic} = −300, −400 mV, V_{ds} = 200 mV. (*F*) Scatterplots of the events detected in the ionic channel. V_{ionic} = −300, −400 mV, V_{ds} = 0 mV. (*G*) τ_{ionic} (median ± SD) versus V_{ionic}. V_{ds} = 0, 200 mV. (*H*) ΔI_{ionic} and ΔI_{diode} (median ± SD) versus V_{ionic}. V_{ds} = 200 mV. The heterojunction stack consists of 3.5 nm thick WSe_2 on top of 2.0 nm thick MoS_2. The pore size was 15 ± 0.3 nm. The DNA molecule was 2,686 bp pUC19 plasmid. The electrolyte was 10 mM KCl in both cis and trans chambers.

bandwidth and higher low-pass filter frequencies is necessary to obtain accurate event statistics that include fast events (37).

The slight increase in ΔI_{ionic} with $|V_{ionic}|$ is consistent with previous studies in dilute salt solutions (38, 39). The relatively small increase in ΔI_{diode} with $|V_{ionic}|$ further supports the charge sensing mechanism, as the effective charge of DNA does not change with V_{ionic} (40).

Potential Improvements. HJD-NP sensors are hypothesized to offer high spatial resolution due to their atomically sharp 2D heterointerfaces. However, this hypothesis has yet to be experimentally validated, which will require a 1 to 2 orders of magnitude improvement in both SNR and dwell time. Strategies to improve the diode's SNR and slow DNA translocation include minimizing series resistances arising from contact and channel resistances through degenerate doping (41–43), reducing background noise by shrinking the overlap region between WSe_2 and MoS_2 from 1 to 10 μm^2 to ≲0.01 μm^2 using nanolithography (41, 44), and enhancing the 2D diode's electrostatic control over DNA by using a smaller nanopore below the Debye screening length (28–31). Additional discussion on slowing DNA translocation and the potential for base-by-base sensing is provided in *SI Appendix, Supplementary Text 5*. Detailed discussion on improving the diode's SNR is provided in *SI Appendix, Supplementary Text 6*.

Conclusion

We demonstrated electrical sensing of DNA translocation through a nanopore using the interlayer current of a vertical 2D diode, concurrently observing slowed transport due to electrostatic

interactions between the DNA and diode. This heterojunction nanopore platform enables sensing capabilities beyond single 2D materials with local out-of-plane electric fields and interlayer currents. The local voltage control V_{ds} is preferred over the global voltage control V_{ionic} to regulate DNA translocation through the nanopore, because i) V_{ds} can be adjusted much more rapidly than V_{ionic}, as the diode channel can potentially operate at GHz frequencies (45) compared to the kHz frequencies of the ionic channel (46), and ii) V_{ds} allows for individual addressing of nanopore sensors in a multiplexed sensor array, which is challenging with V_{ionic}.

Exciting future directions include exploring band-to-band tunneling with type-III band alignment and measuring correlated intralayer currents within each semiconductor layer to complement interlayer measurement. Future work could also add a voltage source between the reference electrode in the electrolyte solution and the diode (19). This modification would enable independent control of the source and drain sides of the diode relative to the solution. By allowing the diode potential to vary with respect to the electrolyte without affecting the potential drop across the diode, this setup could provide enhanced control of DNA translocation. Collectively, the vertical 2D diode nanopore presents promising pathways toward solid-state nanopore sequencing.

Materials and Methods

HJD-NP Device Fabrication. *SI Appendix*, Fig. S1 illustrates the fabrication procedure. The process started with a 20 ± 2 nm thick commercial SiN_x membrane (NBPX4001Y-LR, Norcada) with a 10 × 10 μm window size on a 4 mm large, 10 to 20 Ωcm low-resistivity silicon substrate. A lightly doped silicon substrate was chosen over an intrinsic silicon substrate to prevent electrostatic discharge, which could further reduce the already low yield (47). Next, i) a 10 to 15 nm thick HfO_x layer was deposited onto the front side of the SiN_x membrane at 200 °C using ALD (Savannah S100 ALD system). The thickness of the HfO_x layer was measured using ellipsometry (J.A. Woollam VASE). Following this, ii) the SiN_x was etched from the HfO_x/SiN_x membrane stack using a 60 s XeF_2 gas etch (XACTIX XeF_2 etching system) at 3 Torr (*SI Appendix*, Fig. S2), with the substrate placed upside down on a clean glass slide during etching. ALD HfO_x served as the etch stop. Consequently, the supporting membrane was converted from 20 nm SiN_x to 10 to 15 nm HfO_x, which offers improved wettability (7) and durability (8).

Subsequently, iii) 2 to 5 nm thick MoS_2 and WSe_2 flakes were exfoliated from synthetic crystals (HQgraphene), stacked together, and transferred onto the membrane using the pick-up technique (9). The thickness of exfoliated 2D flakes (MoS_2, WSe_2, and hBN) was optically identified after exfoliation and verified with atomic force microscopy (AFM) after transfer. The size of the WSe_2/MoS_2 overlap region was 1 to 10 μm^2. AFM tip-based cleaning was used to remove surface residues from the transfer process (48). Next, iv) a 100 × 100 μm large, 50 nm thick gold pad was transferred onto the WSe_2 flake as the p-type contact electrode in a N_2-filled glovebox (49). Subsequently, v) 5 nm Ni/30 nm Au was deposited onto the MoS_2 flake as the n-type contact electrode using optical or ebeam lithography followed by ebeam evaporation. Then, vi) a 5 to 20 nm thick hBN flake was exfoliated and transferred onto the membrane to fully encapsulate the WSe_2/MoS_2 heterostructure using the pick-up technique (9). This multilayer hBN flake reduces electron doping and damage to WSe_2 from ALD HfO_x. Next, a gentle remote O_2 plasma process (1 min, 10 W, Tergeo plasma cleaner) was used to nucleate the hBN surface for complete and uniform ALD coverage (50). Afterward, vii) a 10 to 15 nm thick HfO_x layer was deposited onto the front side of the device at 200 °C using ALD for electrical insulation. Leakage tests in *SI Appendix*, Fig. S15 *A* and *B* found a minimum of 10 nm ALD HfO_x was sufficient for electrical insulation. The total thickness of the final membrane stack (HfO_x/hBN/$WSe_2/MoS_2/HfO_x$) was 30 to 60 nm.

Finally, viii) a 1 to 15 nm nanopore was drilled through the membrane stack in the WSe_2/MoS_2 overlap region using a focused electron beam at 300 kV using STEM (Themis Z, Thermo Fisher Scientific). A beam current of 13 nA (4 nA) was required to drill through the membrane stack within a few minutes in nanoprobe (microprobe) mode with spot size 1, corresponding to a beam size of about 1 nm (a few nm). The electron irradiation dose for initial imaging and locating the drilling spot was 10^7 e^-/nm^2 (10^6 e^-/nm^2). After drilling, the nanopore was imaged in STEM with a 30 pA beam current and an atomic beam size (nanoprobe mode with spot size 9).

Cross-Sectional STEM Sample Fabrication and Imaging. A protective layer of 5 to 30 nm thick amorphous carbon was thermally evaporated onto the nanopore device membrane. The cross-sectional STEM sample was then fabricated using standard focused ion beam (FIB) lift-out procedures with a FIB-SEM system (Helios 600i DualBeam, Thermo Fisher Scientific). A cryo-can was used during FIB thinning to minimize redeposition. The cross-sectional sample was imaged using an aberration-corrected STEM (Themis Z, Thermo Fisher Scientific), operated at 300 kV with a convergence angle of 25.2 mrad. Elemental mapping was performed using the Super-X EDS detector.

Photocurrent Mapping. Scanning photocurrent measurements were performed by rastering a focused laser spot across the device surface, using a source measure unit (2450 SourceMeter, Keithley) for voltage sourcing and a current preamplifier (SR570, Stanford Research System) for current measurement. The laser spot had a diameter of 1 μm, a wavelength of 488 nm, and a power of 70 μW.

Raman Measurements. Raman measurements were performed with a confocal Raman microscope (Nanophoton Raman 11) using a 532 nm laser with a 100× objective. Raman spectra were obtained using a grating of 2,400 lines/mm at a laser power of 0.5 mW/cm^2 and an acquisition time of 30 s. Raman maps were obtained using a grating of 2,400 lines/mm at a laser power of 0.5 mW/cm^2, an acquisition time of 3 s/pixel and a pixel size of 300 nm.

Nanopore Measurements and Data Analysis. Before the experiment, the fabricated chip was attached onto a custom-made printed circuit board (PCB) by applying silicone elastomer (Kwik-cast, World Precision Instruments) around the edges of the chip. The silicone elastomer was then further applied around the membrane to reduce the chip capacitance and provide additional insulation between the metal leads and the electrolyte, leaving an exposed area of less than 0.01 mm^2. C_{lead} was 5.2 nF without the silicone paint and 9.2 pF with the silicone paint, measured using triangular V_{ionic} waves (51). Afterward, the chip was electrically connected to the PCB by wire bonding. The PCB was cleaned with acetone, IPA, and deionized (DI) water (18 MΩ cm, Milli-Q, Millipore), and then sandwiched between two chambers of mechanically clamped custom-made PMMA flow cells.

Next, both chambers were sequentially flushed with DI water, IPA, DI water, and a salt solution of 10 mM KCl, 10 mM Tris, 1 mM EDTA at a pH of 7.4 ± 0.2. Both the DI water and salt solution were degassed overnight using a dry scroll vacuum pump (SVF-E3M-20PC, Scroll Labs), which is critical for successful nanopore wetting. In most cases, the nanopore could not be fully wetted immediately. To promote wetting, three methods were employed: i) flushing both chambers with IPA, ii) leaving both chambers with degassed 10 mM KCl solution overnight, and iii) ramping the ionic voltage between ±500 mV in 10 mM KCl.

All current measurements were performed using an integrated patch-clamp amplifier (MultiClamp 700B, Axon Instruments), with channel 1 dedicated to the ionic channel and channel 2 to the diode channel. Channel 1 was connected to a pair of Ag/AgCl electrodes to apply V_{ionic} and measure I_{ionic}. The ionic voltage was applied to the *trans* chamber, while the *cis* chamber was grounded. Channel 2 was connected to the PCB to apply V_{ds} and measure I_d. The electrical voltage was applied to the drain side with p-WSe_2, while the source side with n-MoS_2 was grounded. Current offsets in both channels were adjusted to zero at zero biases. The entire setup was housed in a Faraday cage with a dedicated low-noise ground connection on a vibration isolation table.

After complete nanopore wetting, both V_{ionic} and V_{ds} were varied while measuring I_{ionic} and I_d to study the interactions between the ionic channel and the diode channel. Additional leakage tests in *SI Appendix*, Fig. S15 *C* and *D* established the operation limits of HJD-NPs as $|V_d - V_{ionic}| \leq 600$ mV and $|V_s - V_{ionic}| \leq 600$ mV. The sampling rate was 1 kHz, and the data were low-pass-filtered at 20 Hz using the built-in 8-pole Bessel filter. The output signal was digitized by a Digidata 1440A (Axon Instruments) and recorded using pClamp 10.7 software. Finally, for DNA sensing experiments, 50 nM of 2,686 bp circular dsDNA (pUC19 plasmid, New England Biolabs) was added to the *trans* chamber. The sampling

rate for DNA sensing was 100 kHz. A 2 kHz low-pass 8-pole Bessel filter was applied to both channels to obtain adequate SNRs for event detection and statistical analysis. Blank experiments were conducted at the applied voltages before DNA insertion. Event detection was performed using the open-source Matlab code package Transalyzer (52). Events shorter than 0.25 ms were excluded due to low-pass filtering, which however skews the complete dwell time distribution (37) and constitutes a limitation of this study. Concurrent events were identified when the event start time in both channels differed by 0.5 ms or less. τ_{ionic} and τ_{diode} were determined using the full-width, half-maximum (FWHM) values of the event (52). ΔI_{ionic} and ΔI_{diode} were determined by dividing the event charge deficit by the FWHM time (52). τ_{ionic} and τ_{diode} were analyzed statistically by fitting the event dwell time histogram with a Gaussian peak for $V_{ds} = 200$ mV and an exponential decay for $V_{ds} = 0$ mV. ΔI_{ionic} and ΔI_{diode} were analyzed statistically by fitting the event amplitude histogram with a Gaussian peak.

Yield. After establishing the fabrication protocol, we started device fabrication with 82 SiN_x membranes, out of which 57 reached the final fabrication step. Out of the fabricated devices, 36 (63%) were excluded from liquid measurements due to an insensitive WSe_2/MoS_2 overlap region, as determined by both I−V characteristics and photocurrent mapping, and 13 (23%) failed to fully wet. We managed to perform DNA translocation measurements on nine devices and successfully detected concurrent events in both ionic and diode channels in two devices. *SI Appendix*, Fig. S17 reports concurrent DNA sensing from the other working device, which exhibits a diode current decrease upon DNA translocation, in contrast to the diode behavior shown in Fig. 4, where the diode current increased. Since this device features a modified structure with a strong p-dopant on WSe_2, we attribute its different diode sensing behavior to enhanced p-doping in WSe_2 dominating over n-doping in MoS_2.

This low yield aligns with previously reported challenges in fabricating FET-nanopore devices (16, 17, 53–55), particularly those using 2D materials (*SI Appendix*, Table S2). *SI Appendix*, Table S3 compares the diode current density, noise, and measured or estimated signals and SNRs across all nine devices with DNA sensing measurements, including seven devices with unresolved diode signals and two devices with resolved diode signals. Devices with unresolved diode signals exhibit similar noise levels to those with resolved diode signals but lower current densities, resulting in reduced and ultimately inadequate SNRs. Low diode current density arises from insufficient p-doping in WSe_2 in devices where the electron density in MoS_2 exceeds the hole density in WSe_2 (*SI Appendix, Supplementary Text 4*).

Taken together, the analysis of the devices with both unresolved and resolved diode signals, combined with the DNA sensing data from the device with enhanced p-doping in WSe_2, suggests that high device variability and low yield primarily arise from insufficient doping control in the 2D materials. To make 2D heterojunction diode nanopore a viable technique with sufficient yield and SNR, doping control in each of the 2D layer is essential, which remains a critical challenge not only for 2D nanopores integrated with local electronic sensors but for 2D electronics in general (56). Further discussions on yield and reproducibility limiting processes are provided in *SI Appendix, Supplementary Text 7*. While further measures can be taken to optimize the yield and SNR, we focused on proof-of-principle of electronic out-of-plane DNA sensing and device behavior characterization, which was accomplished in this study.

Data, Materials, and Software Availability. The dataset supporting these findings is openly available in the Illinois Data Bank at https://doi.org/10.13012/B2IDB-7678688_V1 (57).

ACKNOWLEDGMENTS. This work was partially funded by Taiwan Semiconductor Manufacturing Company under Grant No. 089401, the NIH under Grant No. R21HG010701, the NSF through the University of Illinois Urbana-Champaign Materials Research Science and Engineering Center (Illinois MRSEC) under Grant No. DMR-2309037, and funding from University of Illinois Urbana-Champaign to R.B. This work was carried out in part in the Holonyak Micro and Nanotechnology Laboratory and Materials Research Laboratory Central Facilities at University of Illinois Urbana-Champaign. We acknowledge the use of facilities and instrumentation supported by NSF through the Illinois MRSEC under Grant No. DMR-2309037. K.W. and T.T. acknowledge support from the Japan Society for the Promotion of Science Grants-in-Aid for Scientific Research program (Grant Nos. 21H05233 and 23H02052) and World Premier International Research Center Initiative, Ministry of Education, Culture, Sports, Science and Technology, Japan.

Author affiliations: [a]Holonyak Micro and Nanotechnology Laboratory, The Grainger College of Engineering, University of Illinois Urbana-Champaign, Urbana, IL 61801; [b]Department of Mechanical Science and Engineering, The Grainger College of Engineering, University of Illinois Urbana-Champaign, Urbana, IL 61801; [c]Department of Materials Science and Engineering, The Grainger College of Engineering, University of Illinois Urbana-Champaign, Urbana, IL 61801; [d]Research Center for Electronic and Optical Materials, National Institute for Materials Science, Tsukuba 305-0044, Ibaraki, Japan; [e]Research Center for Materials Nanoarchitectonics, National Institute for Materials Science, Tsukuba 305-0044, Ibaraki, Japan; [f]Materials Research Laboratory, The Grainger College of Engineering, University of Illinois Urbana-Champaign, Urbana, IL 61801; [g]Department of Biomedical and Translational Science, The Carle Illinois College of Medicine, University of Illinois Urbana-Champaign, Urbana, IL 61801; [h]Department of Bioengineering, The Grainger College of Engineering, University of Illinois Urbana-Champaign, Urbana, IL 61801; [i]Chan Zuckerberg Biohub Chicago, Chicago, IL 60642; and [j]Carl R. Woese Institute for Genomic Biology, University of Illinois Urbana-Champaign, Urbana, IL 61801

Author contributions: S.C., A.M.v.d.Z., and R.B. designed research; S.C., S.H., E.H., and P.Y.H. performed research; J.S., K.W., T.T., and W.P.K. contributed new reagents/analytic tools; S.C., S.H., E.H., and P.Y.H. analyzed data; A.M.v.d.Z. and R.B. supervised research; and S.C., A.M.v.d.Z., and R.B. wrote the paper.

1. B. M. Venkatesan, R. Bashir, Nanopore sensors for nucleic acid analysis. *Nat. Nanotechnol.* **6**, 615–624 (2011).
2. S. Chen, R. Bashir, Advances in field-effect biosensors towards point-of-use. *Nanotechnology* **34**, 492002 (2023).
3. S. Polonsky, S. Rossnagel, G. Stolovitzky, Nanopore in metal-dielectric sandwich for DNA position control. *Appl. Phys. Lett.* **91**, 153103 (2007).
4. S. Harrer *et al.*, Electrochemical characterization of thin film electrodes toward developing a DNA transistor. *Langmuir* **26**, 19191–19198 (2010).
5. C. H. Lee *et al.*, Atomically thin p–n junctions with van der Waals heterointerfaces. *Nat. Nanotechnol.* **9**, 676–681 (2014).
6. P. V. Pham *et al.*, 2D heterostructures for ubiquitous electronics and optoelectronics: Principles, opportunities, and challenges. *Chem. Rev.* **122**, 6514–6613 (2022).
7. J. Shim, J. A. Rivera, R. Bashir, Electron beam induced local crystallization of HfO_2 nanopores for biosensing applications. *Nanoscale* **5**, 10887 (2013).
8. Y. C. Chou, P. Masih Das, D. S. Monos, D. S. Monos, M. Drndić, Lifetime and stability of silicon nitride nanopores and nanopore arrays for ionic measurements. *ACS Nano* **14**, 6715–6728 (2020).
9. K. Kim *et al.*, Van der Waals heterostructures with high accuracy rotational alignment. *Nano. Lett.* **16**, 1989–1995 (2016).
10. S. H. H. Shokouh *et al.*, High-performance, air-stable, top-gate, p-channel WSe_2 field-effect transistor with fluoropolymer buffer layer. *Adv. Funct. Mater.* **25**, 7208–7214 (2015).
11. M. Puster, J. A. Rodríguez-Manzo, A. Balan, M. Drndić, Toward sensitive graphene nanoribbon-nanopore devices by preventing electron beam–induced damage. *ACS Nano* **7**, 11283–11289 (2013).
12. X. Zhang *et al.*, Van der Waals-interface-dominated all-2D electronics. *Adv. Mater.* **35**, 2207966 (2023).
13. Y. Z. Zhang, G. J. Zhu, J. H. Yang, Origin of p-type conductivity in a WSe_2 monolayer. *Nanoscale* **15**, 12116–12122 (2023).
14. M. D. Siao *et al.*, Two-dimensional electronic transport and surface electron accumulation in MoS_2. *Nat. Commun.* **9**, 1442 (2018).
15. T. Roy *et al.*, Dual-gated MoS_2/WSe_2 van der Waals tunnel diodes and transistors. *ACS Nano* **9**, 2071–2079 (2015).
16. P. Xie, Q. Xiong, Y. Fang, Q. Qing, C. M. Lieber, Local electrical potential detection of DNA by nanowire–nanopore sensors. *Nat. Nanotechnol.* **7**, 119–125 (2012).
17. F. Traversi *et al.*, Detecting the translocation of DNA through a nanopore using graphene nanoribbons. *Nat. Nanotechnol.* **8**, 939–945 (2013).
18. M. Puster *et al.*, Cross-talk between ionic and nanoribbon current signals in graphene nanoribbon–nanopore sensors for single-molecule detection. *Small* **11**, 6309–6316 (2015).
19. S. J. Heerema *et al.*, Probing DNA Translocations with Inplane Current Signals in a Graphene Nanoribbon with a Nanopore. *ACS Nano* **12**, 2623–2633 (2018).
20. M. Graf, M. Lihter, D. Altus, S. Marion, A. Radenovic, Transverse detection of DNA using a MoS_2 nanopore. *Nano. Lett.* **19**, 9075–9083 (2019).
21. J. Feng *et al.*, Electrochemical reaction in single layer MoS_2: Nanopores opened atom by atom. *Nano Lett.* **15**, 3431–3438 (2015).
22. M. Brunet Cabré, A. E. Paiva, M. Velický, P. E. Colavita, K. McKelvey, Electrochemical kinetics as a function of transition metal dichalcogenide thickness. *Electrochim. Acta* **393**, 139027 (2021).
23. S. Banerjee *et al.*, Electrochemistry at the edge of a single graphene layer in a nanopore. *ACS Nano* **7**, 834–843 (2013).
24. M. Niu *et al.*, Light-driven ion transport through single-heterojunction nanopores. *Nano Lett.* **23**, 1010–1016 (2023).
25. Z. Yuan *et al.*, Light-driven ionic and molecular transport through atomically thin single nanopores in MoS_2/WS_2 heterobilayers. *ACS Nano* **18**, 24581–24590 (2024).
26. S. W. Nam, M. J. Rooks, K. B. Kim, S. M. Rossnagel, Ionic field effect transistors with sub-10 nm multiple nanopores. *Nano Lett.* **9**, 2044–2048 (2009).
27. Z. Jiang, D. Stein, Charge regulation in nanopore ionic field-effect transistors. *Phys. Rev. E* **83**, 31203 (2011).

28. Y. Ai, J. Liu, B. Zhang, S. Qian, Field effect regulation of DNA translocation through a nanopore. *Anal. Chem.* **82**, 8217–8225 (2010).
29. Y. Liu, L. Yobas, Slowing DNA translocation in a nanofluidic field-effect transistor. *ACS Nano* **10**, 3985–3994 (2016).
30. P. C. Yen, C. H. Wang, G. J. Hwang, Y. C. Chou, Gate effects on DNA translocation through silicon dioxide nanopore. *Rev. Sci. Instrum.* **83**, 034301 (2012).
31. Y. He, M. Tsutsui, C. Fan, M. Taniguchi, T. Kawai, Controlling DNA translocation through gate modulation of nanopore wall surface charges. *ACS Nano* **5**, 5509–5518 (2011).
32. R. M. M. Smeets *et al.*, Salt dependence of ion transport and DNA translocation through solid-state nanopores. *Nano Lett.* **6**, 89–95 (2006).
33. H. Chang *et al.*, DNA counterion current and saturation examined by a MEMS-based solid state nanopore sensor. *Biomed. Microdevices* **8**, 263–269 (2006).
34. M. Wanunu, J. Sutin, B. McNally, A. Chow, A. Meller, DNA translocation governed by interactions with solid-state nanopores. *Biophys. J.* **95**, 4716–4725 (2008).
35. Y. M. N. D. Y. Bandara, N. Farajpour, K. J. Freedman, Nanopore current enhancements lack protein charge dependence and elucidate maximum unfolding at protein's isoelectric point. *J. Am. Chem. Soc.* **144**, 3063–3073 (2022).
36. L. S. Lastra, Y. M. N. D. Y. Bandara, M. Nguyen, N. Farajpour, K. J. Freedman, On the origins of conductive pulse sensing inside a nanopore. *Nat. Commun.* **13**, 2186 (2022).
37. C.-Y. Lin *et al.*, Ultrafast polymer dynamics through a nanopore. *Nano Lett.* **22**, 8719–8727 (2022).
38. K. J. Freedman *et al.*, Nanopore sensing at ultra-low concentrations using single-molecule dielectrophoretic trapping. *Nat. Commun.* **7**, 10217 (2016).
39. K. Chen, N. A. W. Bell, J. Kong, Y. Tian, U. F. Keyser, Direction- and salt-dependent ionic current signatures for DNA sensing with asymmetric nanopores. *Biophys. J.* **112**, 674–682 (2017).
40. U. F. Keyser *et al.*, Direct force measurements on DNA in a solid-state nanopore. *Nat. Phys.* **2**, 473–477 (2006).
41. S. Chen, Y. Zhang, W. P. King, R. Bashir, A. M. Van Der Zande, Edge-passivated monolayer WSe_2 nanoribbon transistors. *Adv. Mater.* **36**, 2313694 (2024).
42. R. Younas, G. Zhou, C. L. Hinkle, A perspective on the doping of transition metal dichalcogenides for ultra-scaled transistors: Challenges and opportunities. *Appl. Phys. Lett.* **122**, 160504 (2023).
43. S. Chen, Y. Zhang, W. P. King, R. Bashir, A. M. van der Zande, Extension doping with low-resistance contacts for p-type monolayer WSe_2 field-effect transistors. *Adv. Electron. Mater.* 2400843 (2024), 10.1002/aelm.202400843.
44. S. Chen *et al.*, Monolayer MoS_2 nanoribbon transistors fabricated by scanning probe lithography. *Nano Lett.* **19**, 2092–2098 (2019).
45. S. Hong *et al.*, Ultrafast van der Waals diode using graphene quantum capacitance and Fermi-level depinning. *Sci. Adv.* **9**, eadh9770 (2023).
46. Z. Mi *et al.*, Ten thousand recaptures of a single DNA molecule in a nanopore and variance reduction of translocation characteristics. *ACS Nano* **18**, 23243–23252 (2024).
47. K. Healy *et al.*, Fabrication and characterization of nanopores with insulated transverse nanoelectrodes for DNA sensing in salt solution. *Electrophoresis* **33**, 3488–3496 (2012).
48. S. Chen *et al.*, Tip-based cleaning and smoothing improves performance in monolayer MoS_2 devices. *ACS Omega* **6**, 4013–4021 (2021).
49. Y. Liu *et al.*, Approaching the Schottky–Mott limit in van der Waals metal–semiconductor junctions. *Nature* **557**, 696–700 (2018).
50. M. Snure *et al.*, Two-dimensional BN buffer for plasma enhanced atomic layer deposition of Al_2O_3 gate dielectrics on graphene field effect transistors. *Sci. Rep.* **10**, 14699 (2020).
51. A. Balan *et al.*, Improving signal-to-noise performance for DNA translocation in solid-state nanopores at MHz bandwidths. *Nano Lett.* **14**, 7215–7220 (2014).
52. B. Doekemeijer *et al.*, Data analysis methods for solid-state nanopores. *Nanotechnology* **26**, 084003 (2015).
53. S. J. Heerema *et al.*, Probing DNA translocations with inplane current signals in a graphene nanoribbon with a nanopore. *ACS Nano* **12**, 2623–2633 (2018).
54. M. Graf, M. Lihter, D. Altus, S. Marion, A. Radenovic, Transverse detection of DNA using a MoS_2 nanopore. *Nano Lett.* **19**, 9075–9083 (2019).
55. X. Zhu *et al.*, Monolithic integration of vertical thin-film transistors in nanopores for charge sensing of single biomolecules. *ACS Nano* **15**, 9882–9889 (2021).
56. Y. Wang, S. Sarkar, H. Yan, M. Chhowalla, Critical challenges in the development of electronics based on two-dimensional transition metal dichalcogenides. *Nat. Electron* **7**, 638–645 (2024).
57. S. Chen *et al.*, Data from "Detecting DNA translocation through a nanopore using a van der Waals heterojunction diode." Illinois Data Bank. https://doi.org/10.13012/B2IDB-7678688_V1. Deposited 15 April 2025.